



Influence of surface roughness on the reflective properties of snow

Tatiana B. Zhuravleva^{a,*}, Alexander A. Kokhanovsky^b

^a V.E. Zuev Institute of Atmospheric Optics SB RAS, 1, Academician Zuev square, Tomsk 634021, Russia

^b Institute of Environmental Physics, University of Bremen, O. Hahn Allee 1, D-28334 Bremen, Germany

ARTICLE INFO

Article history:

Received 18 October 2010

Received in revised form

24 December 2010

Accepted 5 January 2011

Available online 12 January 2011

Keywords:

Snow roughness

Stochastic radiative transfer theory

Numerical simulation

Albedo

Snow reflection function

ABSTRACT

In this paper the influence of 3D effect on snow reflection function (SRF) and albedo is studied in the framework of the stochastic radiative transfer theory. In particular, the corresponding equations for the averaged intensity of reflected light are solved for the ensemble of realizations of the stochastic field $\kappa(r)$, describing the distribution of 3D elements on the flat semi-infinite snow layer (SISL). The reflection from the underlying SISL is modeled using the solution of the 1D radiative transfer equation. The corresponding look-up tables were compiled beforehand and used in the simulation process. In accordance with the previous studies, it was found that the albedo of snow layer is reduced (in particular, in the infrared region), if 3D effects are taken into account. There is no such a reduction, if light absorption in snow is absent. The 3D effects may increase or decrease SRF depending on the sastrugi fraction and illumination/observation conditions.

© 2011 Elsevier Ltd. All rights reserved.

1. Introduction

Snow is the most reflective surface type on Earth, and it plays an important role in the surface energy budget of polar regions and climate of the globe. Remote sensing, using visible and near-infrared wavelengths, is one of the most suitable techniques for monitoring snow physical parameters. A narrow field-of-view sensor on satellite measures the reflected radiance only in some particular directions. Therefore, the knowledge of angular pattern of bidirectional reflectance distribution function (BRDF) is a crucial factor in accurately retrieving the snow physical parameters from remote sensing data.

At initial research stages, the snow BRDF was simulated based on solution of radiative transfer equation (RTE) in a plane-parallel horizontally homogeneous model [1]. Comparisons with experimental data showed that the measured bidirectional reflectance can markedly differ from model results obtained under assumption of a flat snow surface [2,3]. Inclusion of diversity of particle shapes and

particle surface roughnesses has improved the agreement with measurements [4,5] for flat snow surfaces. However, the predicted RTE bidirectional reflectance still remained more anisotropic, e.g., in the glint region, than the measured one [3,6–10] (in the case of horizontally inhomogeneous snow). This latter has added to recognition that to reconcile the theoretical and experimental results, the calculations should include some other factors and, in particular, the roughness of the snow surface.

The influence of snow roughness on bidirectional reflection has been advanced by several measurement campaigns [3,11–16]. To quantify the snow roughness effect on radiative characteristics, several theoretical models had also been developed [10,15,17,18]. For instance, model [15] approximated the vertical protrusions by rectangular parallelepipeds, elongated in a given direction and located on a flat anisotropic surface. Lyapustin et al. [10] have suggested a model of macroscopic snow surface roughness, capable to account for the presence, on smooth snow, of non-horizontal surfaces, bounding roughness elements, and to reduce the fraction of surface-reflected radiation on the basis of a simple shadow model. Reflectance of an individual facet was simulated on the basis of RTE for a horizontally homogeneous plane-parallel medium, with

* Corresponding author.

E-mail address: ztb@iao.ru (T.B. Zhuravleva).

a subsequent averaging over the slope distribution function; the shadowing effect was accounted for using an approximation of shadowed area by hemispheric protrusions with a fixed center-to-center distance.

These studies showed that the inclusion of snow roughness in the radiance calculations reconciles the model and experimental results (in particular, the roughness reduces the brightness of glint region and enhances the backscattering), but so far a considerable discrepancy exists between the modeled effects and observations, indicating the need for further model refinement. As a continuation of these studies, here the snow roughness effect on reflected radiation is suggested to be described with a *statistical approach*.

The expedience of the statistical approach stems from the fact that the available information on the roughness of the underlying surface, containing large number of macro-inhomogeneities, is insufficient for unique determination of the reflected radiation at an arbitrary point of phase space of coordinates and directions. However, it is possible to make practice-important conclusions about the average (over ensemble of realizations of surface inhomogeneities) characteristics of reflected radiation, i.e., to determine and analyze the interrelation between the statistical characteristics of inhomogeneous underlying surface and radiation. One of the promising methods of realization of the statistical approach is the technique based on the numerical or analytical averaging of stochastic RTE over the ensemble of rough surface fragments. The variant of realization of this approach, as applied to the problem of the solar radiative transfer in *clouds*, was first formulated by Avaste and Vainikko [19]. The development of the statistical approach was furthered by Titov [20,21], who created the constructive optical models of cloud fields with random geometry using the Poisson ensembles of points in space and on the straight lines.

Though developed initially to treat the optical radiative transfer in stochastic clouds, the models [20,21] can help to develop the transfer theory for other optically macro-inhomogeneous scattering and absorbing media (roughed sea surface, mountain system with random distribution of heights and normals, etc.). In particular, prevailing wind direction in polar regions favors formation of sastrugi, i.e., narrow and hard snow ridges up to a few meters long and from a few centimeters to 20–25 cm tall [2,15,16]. They alternate with wind grooves, appearing as dense snow is eroded by wind-blown snow particles. Sastrugi are often encountered on vast smoothed territories, blown by permanent strong winds, particularly on slopes of large glacial covers. (In analogy with [16], we take “sastrugi” as a plural noun and “sastruga” as a singular noun to mean a single element in a field of sastrugi.) As a first approximation, the sastrugi can be modeled as rectangular parallelepipeds with random horizontal sizes and a fixed height H . The roughness effect, due to sastrugi presence, on the reflected radiance can be described using a statistically homogeneous model on the basis of Poisson point fluxes on the straight lines.

We also note that snow layer is a multiple scattering close-packed medium with irregularly shaped non-uniform grains. Use of the radiative transfer theory, developed under the assumption that scattering particles are located in each

other's far-field zones and are uncorrelated, in the case of densely packed particles can lead to significant deviations from the numerical predictions based on the RTE [22]. However, rigorous analytical theory of electromagnetic energy transport in densely packed particulate media is still at its development stage (see, e.g., [23,24]). In addition, wave effects are weak for snow in view of large size of particles as compared to the wavelength, weak absorption, strong multiple scattering, irregular shapes of particles and can be ignored as far as practical aspects of remote sensing are of concern. In this regard, many research groups (see, e.g., [1,14,25,26,27,28]) used the classical RTE – as an approximate methodology – to calculate the radiative characteristics in densely packed media. Summarizing, we will, too, not consider the close-packed effects in this paper.

This paper is organized as follows. Section 2 presents the main notations used in the paper. Section 3 describes the model and methods of calculating the average fluxes and intensities. Section 4 contains the data on the characteristic optical and geometrical parameters of sastrugi. Influence of 3D effects on the radiative characteristics of the rough snow surface is discussed in Sections 5 (albedo) and 6 (angular structure of reflected radiation).

2. Main notations

We will introduce the main notations.

An individual sastruga is approximated by rectangular parallelepiped with height H and random horizontal sizes D'_x and D'_y along the OX and OY axes, respectively (Fig. 1). The average horizontal sastrugi sizes within the considered region will be denoted through D_x and D_y , and the part of the region occupied by sastrugi will be denoted through SF (sastrugi's fraction, or sastrugi density). The sastrugi are assumed to be elongated along a certain given direction (such as, in the direction of OX axis, Fig. 2a); and the roughnesses are described using, in addition to D_x , D_y , and H , also their ratios: $\beta = D_x/D_y$ and $\gamma = H/D_y$. Thus, the parameter γ (aspect ratio) characterizes the ratio of the sastrugi height to the mean sastrugi size in non-dominant direction (along OY axis). The optical characteristics of

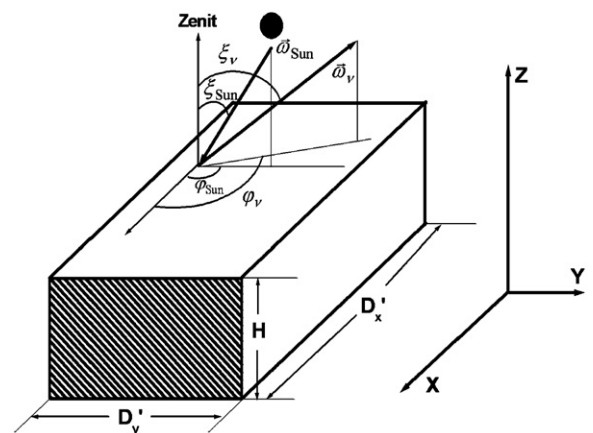


Fig. 1. Illumination (\vec{r}_{Sun}) and viewing (\vec{r}_v) conditions of sastruga, located on a flat surface; the sastruga is approximated by a rectangular parallelepiped with the horizontal sizes D'_x and D'_y and constant height H .

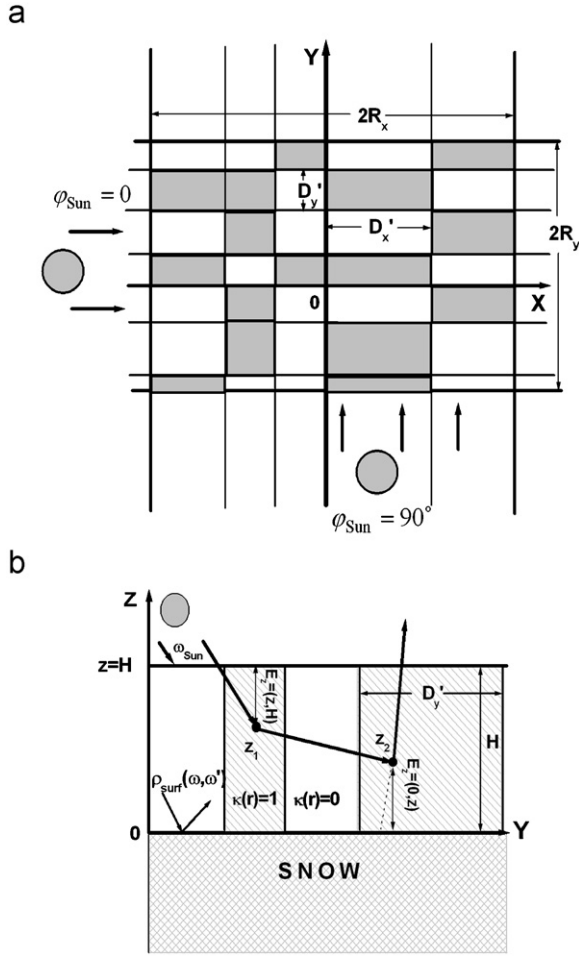


Fig. 2. (a) A schematic realization of the model on the basis of Poisson point fluxes on the straight lines in the XOY-plane and (b) illustration of radiation propagation in the layer A (cross-section in the YOZ-plane).

snow, composing the sastrugi, are as follows: extinction coefficient $\sigma(\vec{r})$, single scattering albedo $\omega_0(\vec{r})$, and scattering phase function $p(\vec{\omega}, \vec{\omega}', \vec{r})$, where $\vec{r} = (x, y, z)$ is the position vector, and $\vec{\omega}$ and $\vec{\omega}'$ are unit vectors.

The vector of incident solar rays $\vec{\omega}_{\text{Sun}}$ is described by the zenith ξ_{Sun} and azimuth φ_{Sun} angles, and its direction cosines are equal respectively to $a_{\text{Sun}} = \sin \xi_{\text{Sun}} \cos \varphi_{\text{Sun}}$, $b_{\text{Sun}} = \sin \xi_{\text{Sun}} \sin \varphi_{\text{Sun}}$, $\mu_{\text{Sun}} = -\cos \xi_{\text{Sun}}$. The unit vector of observations $\vec{\omega}_v$ is characterized by the zenith ξ_v and azimuth φ_v angles with the corresponding direction cosines $a_v = \sin \xi_v \cos \varphi_v$, $b_v = \sin \xi_v \sin \varphi_v$, and $\mu_v = \cos \xi_v$ (see Fig. 1).

The coefficient of reflection from semi-infinite snow layer (SISL), on which the sastrugi are located, will be denoted through $\rho_{\text{surf}}(\vec{\omega}, \vec{\omega}')$. The vector of incident radiation $\vec{\omega}$ (the vector $\vec{\omega}'$, characterizing the direction of reflected radiation) is defined by zenith ξ (ξ') and azimuth φ (φ') angles, and its direction cosines are equal to $a = \sin \xi \cos \varphi$ ($a' = \sin \xi' \cos \varphi'$), $b = \sin \xi \sin \varphi$ ($b' = \sin \xi' \sin \varphi'$), and $\mu = -\cos \xi$ ($\mu' = \cos \xi'$).

The relative azimuth angle between sastrugi elongation direction φ_{sas} (along the OX axis: $\varphi_{\text{sas}} = 0^\circ$, Fig. 2a) and

incidence direction of solar rays φ_{Sun} is denoted as $\varphi_{\text{Sun}-\text{sas}} = \varphi_{\text{Sun}} - \varphi_{\text{sas}}$. The $\varphi_{\text{Sun}} = 0^\circ$ and $\varphi_{\text{Sun}} = 90^\circ$ cases correspond to situations when the incident light direction is parallel ($\varphi_{\text{Sun}-\text{sas}} = 0^\circ$) and perpendicular ($\varphi_{\text{Sun}-\text{sas}} = 90^\circ$) to the sastrugi elongation direction, respectively (Fig. 2a).

3. Theory

The optical model of snow roughness is specified in the layer $A = (0 \leq z \leq H)$ (z is the vertical coordinate and H is the height of roughness elements, see Fig. 2b) in terms of the random scalar fields of extinction coefficient $\sigma(\vec{r})\kappa(\vec{r})$, single scattering albedo $\omega_0(\vec{r})\kappa(\vec{r})$, and scattering phase function $p(\vec{\omega}, \vec{\omega}', \vec{r})\kappa(\vec{r})$. The stochasticity of the snow roughness is described by the random indicator function

$$\kappa(\vec{r}) = \begin{cases} 1, & \vec{r} \in G \\ 0, & \vec{r} \notin G \end{cases}, \quad (3.1)$$

where G is a random set of points in the layer A , at which snow is present, i.e., $\kappa(\vec{r}) = 1$ inside sastrugi and $\kappa(\vec{r}) = 0$ outside them.

Under assumption that the optical radiation does not interact with the gas-aerosol atmosphere within the layer A , the stochastic scalar RTE with respect to the random intensity $I(\vec{r}, \vec{\omega})$ at the point \vec{r} in the direction $\vec{\omega}$ has the form

$$\vec{\omega} \nabla I(\vec{r}, \vec{\omega}) + \sigma(\vec{r})\kappa(\vec{r})I(\vec{r}, \vec{\omega}) = \omega_0(\vec{r})\sigma(\vec{r})\kappa(\vec{r}) \int_{4\pi} p(\vec{\omega}, \vec{\omega}', z)I(\vec{r}, \vec{\omega}')d\vec{\omega}'. \quad (3.2)$$

After inversion of the integro-differential operator (see, e.g., [19,20,29]), this equation in the Cartesian coordinate system OXYZ is represented as

$$\begin{aligned} I(\vec{r}, \vec{\omega}) + \frac{1}{|\mu|} \int_{E_z} \sigma(\vec{r}')\kappa(\vec{r}')I(\vec{r}', \vec{\omega}')dz' \\ = \frac{1}{|\mu|} \int_{E_z} \omega_0(\vec{r}')\sigma(\vec{r}')\kappa(\vec{r}') \int_{4\pi} p(\vec{\omega}, \vec{\omega}', z')I(\vec{r}', \vec{\omega}')d\vec{\omega}'dz' \\ + I_*(\vec{r}, \vec{\omega}) \end{aligned} \quad (3.3)$$

where $I_*(\vec{r}, \vec{\omega})$ is the radiance of external sources at the layer boundaries and (Fig. 2b)

$$E_z = \begin{cases} (0, z), & \mu > 0 \\ (z, H), & \mu < 0 \end{cases}. \quad (3.4)$$

The boundary condition for (3.3) on the upper boundary $z=H$ of the layer is given by

$$I_*(\vec{r}, \vec{\omega}) = I^\downarrow(z=H, \vec{\omega}) = F_0 \delta(\vec{\omega} - \vec{\omega}_{\text{Sun}}), \quad (3.5)$$

where F_0 is the incident flux per unit area perpendicular to the incident (\downarrow) beam. The boundary condition for (3.3) on the lower boundary $z=0$ of the layer corresponds to the radiation, reflected (\uparrow) from the underlying surface with the reflection coefficient $\rho_{\text{surf}}(\vec{\omega}, \vec{\omega}')$:

$$I^\uparrow(z=0, \vec{\omega}) = \frac{1}{\mu} \int_{2\pi} \rho_{\text{surf}}(\vec{\omega}, \vec{\omega}')|\mu'|I^\downarrow(z=0, \vec{\omega}')d\vec{\omega}' \quad (3.6)$$

The mathematical model of the $\kappa(\vec{r})$ field is constructed based on the Poisson point fluxes on straight lines as described, for instance, by Titov [20]. It is briefly discussed below.

3.1. Model based on the Poisson point fluxes on straight lines

We assume that the values of the indicator function $\kappa(\vec{r})$ do not depend on z (the $\kappa(\vec{r})$ field is *statistically homogeneous*). Then, in the plane $z=0$ within the simulation region shaped as a rectangle with sides $2R_x$ and $2R_y$ and centered at origin $([-R_x, R_x] \times [-R_y, R_y])$, a random field $\xi(\vec{v})$, $\vec{v} = (x, y)$, is constructed as follows (Fig. 2a):

- on the OX and OY axes, we construct the Poisson point fluxes $\{x_i\}$ and $\{y_j\}$ with the intensities A_x and A_y (numbers of points per unit length), respectively;
- in each rectangle $[x_i, x_{i+1}] \times [y_j, y_{j+1}]$, the random field $\xi(\vec{v})$ takes the value “1” (presence of sastruga) with the probability P and the value “0” (absence of sastruga) with the probability $(1-P)$. Values of the indicator function for each rectangle are chosen independently.

Thus, to construct a realization of $\kappa(\vec{r}) = \xi(\vec{v})$, we need to specify the probability of sastruga presence P and the intensities of the Poisson fluxes A_x and A_y , whose values are logical to relate with the sastruga parameters measured in field experiments. In analogy with the way it was made in the Poisson model of *broken clouds*, we will use, as P , the quantity $P=SF$. The intensities of the Poisson fluxes (for a fixed SF) will be defined using the formulas $A_{x(y)} \sim 1/D_{x(y)}$. (In this work, the intensities of the Poisson flux A_x and A_y are specified using formulas (see Appendix A), obtained earlier for the cloud fields with random geometry [21].)

A realization of the sastruga field, constructed according to the above scheme, represents a set of rectangular parallelepipeds, located on a flat Lambertian or anisotropic surface and having identical geometrical thickness H and random horizontal sizes (Fig. 2). The intensities $\langle I(z, \vec{\omega}) \rangle$ and fluxes $\langle F(z) \rangle$, average over the ensemble of realizations of surface inhomogeneities, can be calculated using two approaches: method based on the numerical simulations and the method of closed equations. Angular brackets will be used to designate ensemble averages over the field realizations.

3.2. Method based on numerical simulations

In essence, the approach consists of

- simulation of a realization of rough surface $\kappa(\vec{r})$;
- calculation of radiation characteristics within a given realization (solution of RTE by the Monte Carlo method); and
- averaging of the obtained results over the set of realizations.

The most computer time demanding part of the algorithm is associated with a sampling realization of $\kappa(\vec{r})$ and with the solution of the RTE in three-dimensional scattering and absorbing medium with a complex and irregular geometry. The efficiency of the $\langle I(z, \vec{\omega}) \rangle$ and $\langle F(z) \rangle$ simulation can be increased with the help of

randomization [30]. An undoubted advantage of the numerical simulation method is that it can account for all the effects associated with random roughness geometry: (i) incident radiative flux may enter, and unscattered and diffuse radiation may exit through the lateral (non-horizontal) surfaces, bounding separate elements of the rough surface; (ii) incident radiation may be screened by surrounding elements; and (iii) individual elements of the rough surface may interact with each other, i.e., the radiation, leaving through a lateral surface, can be multiply scattered by the surrounding sastrugi [20,21].

We note that the numerical simulation method can be used not only for the above-mentioned model, but also for any constructive model of $\kappa(\vec{r})$, such as when the indicator function is described on the basis of the model of Poisson point fluxes in space [20]. In this latter case, the roughnesses are approximated by simple geometric bodies (inverted truncated paraboloids, truncated spheres and ellipsoids, etc.), and the number of their centers in two-dimensional simulation region is determined in accordance with the Poisson law.

3.3. Method of closed equations (MCE)

The derivation of closed system of equations with respect to the average intensity $\langle I(\vec{r}, \vec{\omega}) \rangle$ and auxiliary function $W(\vec{r}, \vec{\omega}) = \langle \kappa(\vec{r}) I(\vec{r}, \vec{\omega}) \rangle$ is given in [20,21]. The first equation is obtained after averaging of the stochastic RTE (3.3) over the ensemble of realizations of the $\kappa(\vec{r})$ field, and the second equation is obtained after multiplying (3.3) by $\kappa(\vec{r})$ and subsequent averaging under assumption of factorization of n -dimensional probability of sastruga presence. We will consider a particular case when, within the layer A ,

- (a) the $\kappa(\vec{r})$ field is statistically homogeneous (the unconditional probability $P(\vec{r}) = P = \text{const}$) and the conditional probability $V(\vec{r}_1, \vec{r}_2)$ that $\kappa(\vec{r}_1) = 1$, given that $\kappa(\vec{r}_2) = 1$, is exponential

$$V(\vec{r}_1, \vec{r}_2) = P + (1-P)\exp(-A|\vec{r}_1 - \vec{r}_2|), \quad (3.7)$$

where A is a parameter, inversely proportional to the characteristic inhomogeneity size;

- (b) the optical characteristics are constant

$$\sigma(\vec{r}) = \sigma, \quad \omega_0(\vec{r}) = \omega_0, \quad p(\vec{\omega}, \vec{\omega}', \vec{r}) = p(\mu_s)/(2\pi), \quad \mu_s = (\vec{\omega}, \vec{\omega}'); \quad (3.8)$$

- (c) the boundary conditions are uniform and are described by Eqs. (3.5)–(3.6).

We introduce a function $f(\vec{x}) = \sigma \langle \kappa(\vec{r}) I(\vec{r}, \vec{\omega}) \rangle$. The idea used to solve the obtained system of closed equations with respect to $\langle I(\vec{r}, \vec{\omega}) \rangle$ and $W(\vec{r}, \vec{\omega})$ is that, under the above assumptions (a)–(c), the function $f(\vec{x})$ satisfies a certain integral equation

$$f(\vec{x}) = \int_X k(\vec{x}', \vec{x}) f(\vec{x}') d\vec{x}' + \psi(\vec{x}), \quad (3.9)$$

where X is the phase space of coordinates and directions $\vec{x} = (\vec{r}, \vec{\omega})$, and the average intensity is represented as a

linear functional

$$\langle I(\vec{r}, \vec{\omega}) \rangle = J_h = (f, h). \quad (3.10)$$

This latter allows us to use the general theory of the Monte Carlo methods for the J_h estimation [31].

In the framework of the model on the basis of the Poisson point fluxes on the straight lines (Section 3.1), condition (3.7) is fulfilled. If we assume that the optical characteristics of sastrugi are constant (see (3.8)), then the requirements necessary to construct the functional (3.10) are met, and the average fluxes $\langle F(\vec{r}) \rangle = \langle F(z) \rangle$ and the intensities $\langle I(\vec{r}, \vec{\omega}) \rangle = \langle I(z, \vec{\omega}) \rangle$ can be calculated on the basis of MCE. In this case, the generalized kernel $k(\vec{x}', \vec{x})$ and the free term $\psi(\vec{x})$ in Eq. (3.9) have the form [20,21]

$$k(\vec{x}', \vec{x}) = \omega_0 p(\mu_*) \sum_{i=1}^2 D_i \eta_i \exp\{-\eta_i |\vec{r} - \vec{r}'|\} \delta\{\vec{\omega} - ((\vec{r} - \vec{r}')/|\vec{r} - \vec{r}'|)\} / (2\pi |\vec{r} - \vec{r}'|^2) \quad (3.11)$$

and

$$\psi(\vec{x}) = \sum_{i=1}^2 C_i \eta_i \exp\{-\eta_i |\vec{r} - \vec{r}_H|\} \delta(\vec{\omega} - \vec{\omega}_{\text{Sun}}), \quad (3.12)$$

\vec{r}_H is a point on the plane $z = H$.

The quantities C_i , D_i , and η_i , $i = 1, 2$, depend on σ , $A_{x(y)}$, P and are calculated according to the formulas presented in Appendix A.

The linear functional (3.10), in accordance with [20], is represented as

$$\langle I(z, \vec{\omega}) \rangle = \frac{\omega_0}{2\pi |\mu|} \int_{E_z} \sum_{i=1}^2 D_i \exp\{-\eta_i |z - z'|/|\mu|\} dz' \times \int_{4\pi} p(\mu_*) f(z', \vec{\omega}) d\vec{\omega}' dz' + \langle j(z, \vec{\omega}) \rangle \delta(\vec{\omega} - \vec{\omega}_{\text{Sun}}), \quad (3.13)$$

where the average flux of unscattered radiation is equal to

$$\langle j(z, \vec{\omega}) \rangle = \sum_{i=1}^2 C_i \exp\{-\eta_i |z - H|/|\mu_{\text{Sun}}|\}. \quad (3.14)$$

The original statistical algorithms for estimating the linear functional (3.13) have been developed and described in detail in [20,21] for the case of an isolated cloud layer, and in [32–34] with inclusion of the interaction of optical radiation with aerosol–gas atmosphere and underlying surface reflecting according to the Lambert law. The comparison with the calculations made using numerical simulation method shows that the approximate equations for mean intensity, obtained with certain limitations on the probabilistic properties of cloud fields, have sufficiently high accuracy [20]. This means that the MCE calculations of the average radiative characteristics capture the effects of the roughness geometry, which were described above. This approach, based on the analytical averaging of RTE, is more efficient from the viewpoint of computer time; therefore, precisely this approach will be used in our subsequent calculations.

This work disregards the interaction of solar radiation with aerosol, enabling identification of the “pure” 3D effects of snow roughness. Use of this approximation is

justified in analysis of ground-based measurements of reflectance and albedo of snow cover in polar regions, where the atmospheric aerosol depth is small. Moreover, we will confine ourselves to consideration of the spectral intervals within which the Rayleigh scattering is small and the molecular absorption can be neglected.

Our algorithms allow us to account for the reflection from the underlying surface both in accordance with the Lambert law, and to account for the anisotropy of semi-infinite horizontally homogeneous snow layer. The main formulas for calculating the average fluxes $\langle F(z) \rangle$ and intensities $\langle I(z, \vec{\omega}) \rangle$ are presented in Appendix A. To convert to the ensemble average snow reflection function (SRF) of the “flat surface–sastrugi” system $\langle R(\vec{\omega}, \vec{\omega}') \rangle$, we use the formula (see, e.g., [4,10,26])

$$\langle R(\vec{\omega}, \vec{\omega}') \rangle = \langle I(z = H, \vec{\omega}') \rangle \pi / (|\mu_{\text{Sun}}| \times F_0). \quad (3.15)$$

Henceforth, the angular brackets will be dropped.

4. Characteristics of sastrugi

To simulate the radiation processes, it is necessary to specify a set of the input parameters, characterizing the snow optical characteristics and geometrical properties of roughness:

- the extinction coefficient σ , the single scattering albedo ω_0 , the scattering phase function $p(\mu_*)$;
- the coefficient of reflection from the underlying flat horizontally homogeneous surface $\rho_{\text{surf}}(\vec{\omega}, \vec{\omega}')$;
- the mean horizontal sastrugi sizes D_x and D_y , the sastrugi height H ; and
- sastrugi density SF .

The synchronous measurements of radiation, snow optical properties, and geometrical characteristics of sastrugi are scarce; therefore, input parameters will be specified using information on the typical sastrugi characteristics in Antarctica, obtained as part of separate campaigns.

4.1. Snow optical characteristics

Here, we will consider a simplified model, assuming that

- flat surface is approximated by SISL; although some works (see, e.g., [35–37]) treat the smooth snow surface as a set of the layers, each with specific optical characteristics, depending on the particle shape and size; and
- optical characteristics of snow (σ , ω_0 , $p(\mu_*)$), that composes the sastrugi, and optical characteristics of snow cover, on which the sastrugi are located, are identical.

It is known that the snow single scattering characteristics depend strongly on the crystal shape and size. Some works [1,38–42] showed that the assumption of sphericity of ice particles and, as a consequence, employment of

the apparatus of the Mie theory are admissible when model calculations and snow albedo measurements are jointly analyzed. At the same time, Leroux et al. [43] found significant improvement to reflection function when using hexagonal crystals in the model rather than spheres with Mie scattering phase function. Stroeve and Nolin [44] also reported errors in bidirectional reflection when a Mie phase function is used with spheres in this type of model. In this regard, for the calculation of the optical and radiative characteristics the use of the non-spherical models is preferable (as far as possible) [4,26,45–47]. Calculation of single scattering properties for various ice crystal shapes has seen much progress in past decade, mostly motivated by the remote sensing of ice clouds. At present, these models are used to specify the optical characteristics of *snow particles* shaped as aggregate grains, columns, etc. [3,5].

Wiscombe and Warren [1], after survey of a wide variety of works published in 1950–1970s, have suggested average grain radii in the range 20–100 μm for new snow, 100–300 μm for fine-grained older snow, and 1–1.5 mm for old snow near melting point. Similar size variability range of *snow particles* was obtained in later experiments in different Antarctic regions [48,49].

In conformity with the studies cited above, the reflected radiation calculations in this work are performed for $\sigma=1\text{ mm}^{-1}$ (when the sastrugi height $H=100\text{ mm}$, the optical depth $\tau=100$) and $0.98 \leq \omega_0 \leq 1$. The scattering phase function $p(\mu_*)$ corresponds to that [26] for particles having highly irregular, random fractal shapes as introduced in [50], with effective size 50 μm , and asymmetry factor $\langle \cos \theta \rangle = 0.76$. The simulation of $\rho_{\text{surf}}(\vec{\omega}, \vec{\omega}')$ is performed on the basis of numerical solution of Ambartsumyan nonlinear integral equation [26]. It was assumed that

$$\rho_{\text{surf}}(\vec{\omega}, \vec{\omega}') = \rho_{\text{surf}}(\zeta, \varphi, \zeta', \varphi') = \rho_{\text{surf}}(\zeta, \zeta', \varphi - \varphi'); \quad (4.1)$$

the cosines of zenith incidence/reflection angles and azimuth angle $(\varphi - \varphi')$ were varied with the steps 0.05 and 10° , respectively, in the corresponding look-up tables.

4.2. Geometrical characteristics of sastrugi

Typical summertime sastrugi sizes at South Pole are presented in [16]. Those results suggest that the ratio of the horizontal sizes β depends on D_x : the horizontal sizes are comparable ($\beta \sim 1$ –2) when sastrugi extents are small ($D_x \leq 4\text{ m}$), and the ratio β increases to 3–10 for larger values of sastrugi extents ($D_x > 5\text{ m}$). The sastrugi height H varies in the range 10–25 cm and the aspect ratio γ is about 0.1.

Sturn et al. [51] reported lengths of snow-surface features in Bellingshausen, Amundsen, and Ross Seas ranging from 3 to 70 m, average being 12.7–23.3 m, depending on the season; the average structural amplitude was within 0.1 m. In accordance with [3], the highest sastrugi were 6–8 cm above the mean surface. Li and Zhou [36] reported that the snow-surface had centimeter-to-decimeter-scale roughness.

Based on this information, the calculations below were performed for $D_x=10\text{ m}$, $D_y=1\text{ m}$, and $H=0.1\text{ m}$ ($\beta=10$, $\gamma=0.1$).

5. Results of numerical simulations of the snow albedo with account for 3D effects

5.1. 3D effects

The 3D effects on the solar radiative transfer in *broken clouds* (cloud fraction $CF < 1$) have been extensively studied by different research groups for a number of last decades (see, e.g., [20,21,29,33,52–57]). At the same time, there are not so many papers aimed to study the 3D effects of *snow roughness* on the basis of numerical simulations, when the variations of the characteristics of snow roughness are available for estimations of the radiative characteristics [10,15,16]. We note that the features of the 3D effects of snow roughness can be compared, in some cases, with 3D effects in clouds, such as when these last overly a strongly reflecting surface or when radiative transfer in clouds with rough top boundary is considered. In particular, Loeb et al. [58] used a three-dimensional Monte Carlo model to compare the reflectance of overcast scenes from plane-parallel clouds to that from clouds with cloud-top height variations. Their results show that the presence of cloud-top height variations reduces the forward reflectance, by up to 30% in their cases, and slightly enhances the backward reflectance, by up to 10%. Despite the fact that the cloud optical depth variations were far smaller than those on the Antarctic snow surface and clouds were underlain by a black surface, these results again show that roughness reduces forward reflectance and enhances backward reflectance.

The effect of snow roughness will be studied by comparing the albedo of SISL (A_{flat}) and albedo of the “flat surface–sastrugi” system (A_{3D}):

$$A_{\text{flat}(3D)} = \frac{1}{\pi} \int_0^{2\pi} \int_0^{\pi/2} R_{\text{flat}(3D)}(\zeta_{\text{Sun}}, \varphi_{\text{Sun}}, \zeta', \varphi') \cos \zeta' \sin \zeta' d\zeta' d\varphi'. \quad (5.1)$$

The albedo of the “flat snow–sastrugi” system is a sum of two components

$$A_{3D} = A_{3D}^{(0)} + A_{3D}^{(\text{sur})}, \quad (5.2)$$

where $A_{3D}^{(0)}$ is the albedo of the layer A , calculated by assuming that reflection from the underlying surface $z=0$ is absent; and $A_{3D}^{(\text{sur})}$ is the contribution to A_{3D} , made by radiation which, during propagation, experienced at least one reflection from flat snow.

We will now consider the factors governing the behavior of $A_{3D}^{(0)}$ and $A_{3D}^{(\text{sur})}$. The results of calculations are shown in Fig. 3. The value of $A_{3D}^{(\text{sur})}$ is determined by the amounts of unscattered and diffuse radiation, having reached the surface $z=0$. For a fixed sastrugi density SF , the fraction of direct radiation is reduced, because of the shadowing effects. As an example, for the parameters indicated in the caption of Fig. 3, at the sastrugi density larger than $SF \sim 0.7$, the direct radiation does not reach the plane $z=0$ at all (see Appendix B), and the behavior of $A_{3D}^{(\text{sur})}$ is determined only by the diffuse radiation, including the

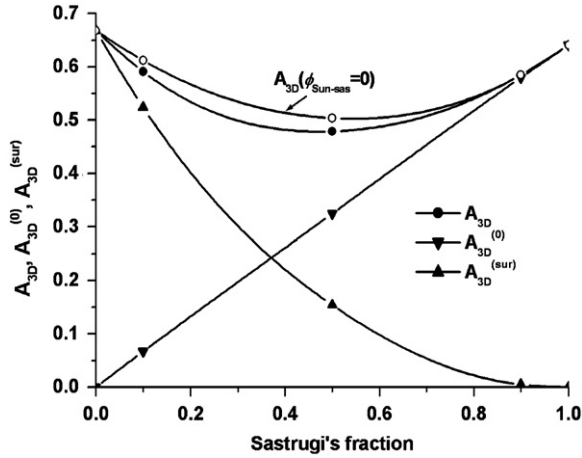


Fig. 3. Albedo of the “flat snow-sastrugi” system and its components $A_{3D}^{(0)}$ and $A_{3D}^{(sur)}$. The sastrugi parameters are: the horizontal sizes $D_x=10$ m, $D_y=1$ m, the height $H=10$ cm, $\sigma=1$ mm $^{-1}$, $\omega_0=0.98$; and $\zeta_{Sun}=75^\circ$, $\varphi_{Sun-sas}=90^\circ$. The upper curve corresponds to the relative Sun-sastrugi azimuth angle equaling zero.

reflection from shadowed sections. Moreover, in the non-conservative scattering case, the photons, experiencing collisions within sastrugi before interaction with the smooth surface, and a part of photons, reflected from the surface $z=0$, may be absorbed within sastrugi. Therefore, we can expect that the $A_{3D}^{(sur)}$ value will decrease with an increase of the sastrugi density.

At the same time, the $A_{3D}^{(0)}$ component is a monotonically increasing function of the sastrugi fraction. For fixed illumination conditions, growth of $A_{3D}^{(0)}$ with an increase of SF is caused by increase, on the average, of the fraction of scattered radiation; and for large SF values, when the distance between the sastrugi, on the average, becomes smaller, a marked role is played by the radiation interaction: a part of the radiation, leaving through the side surfaces, may be multiply scattered by the neighboring sastrugi [21].

Thus, for small sastrugi density ($SF \sim 0.1$ – 0.2), the main contributor to A_{3D} is radiation reflected from the flat surface. For large SF values ($SF > 0.7$ – 0.8), the albedo is dominated by absorption and scattering processes, taking place immediately within the layer A positioned above the underlying flat snow surface (Fig. 3).

Overall, the numerical simulation results, obtained in the framework of the used sastrugi model, showed that, when $\omega_0 < 1$,

- the albedo of the rough snow cover is not larger than the albedo of the flat layer: $A_{3D}(SF > 0) \leq A_{flat}$;
- the albedo of the “flat snow-sastrugi” system has a minimum achieved for moderate sastrugi densities ($SF \sim 0.5$ – 0.6);
- for small to moderate SF values, the albedo of the rough snow is less in the case when direct solar rays are incident perpendicular to the sastrugi elongation direction than in the case of incidence along the elongation direction (Fig. 3): $A_{3D}(\varphi_{Sun-sas}=90^\circ) \leq A_{3D}(\varphi_{Sun-sas}=0)$. Partly, this is because the sections of the flat snow,

which are illuminated by unscattered solar radiation, decrease in area. As SF increases, the difference between the albedos of rough and smooth surfaces is reduced.

5.2. Influence of the sastrugi parameters, density and the illumination conditions on the albedo of the “flat snow-sastrugi” system

This section discusses the effect of factors, governing the average albedo of the “flat snow-sastrugi” system (illumination conditions, sastrugi density, optical and geometrical characteristics). For a quantitative description of 3D effects on the average albedo A_{3D} compared to the SISL albedo, we use the quantity:

$$\Delta_{3D} = 100\% \times ((A_{3D} - A_{flat}) / A_{flat}). \quad (5.3)$$

A detailed dependence of A_{3D} and Δ_{3D} on snow single scattering albedo under illumination conditions, when the 3D effects are most significant ($\varphi_{Sun-sas}=90^\circ$), is presented in Fig. 4. When snow absorptance is weak ($\omega_0=0.9999$), appearance of sastrugi produces a decrease of A_{flat} by no more than 0.02–0.03, and $|\Delta_{3D}|$ is less than 2–3%. In the near-IR spectral region, A_{3D} decreases and the 3D effects of roughnesses substantially intensify, reaching a few tens of percent: in particular, $|\Delta_{3D}| \approx 30\%$ at $\omega_0=0.98$. The largest deviations $|\Delta_{3D}|$ take place for moderate sastrugi fractions; e.g., for $\omega_0=0.98 \div 0.995$ the maximum values are attained at $SF \sim 0.5$, whereas for $0.999 \leq \omega_0 < 1$ the maximum shifts toward the region $SF \sim 0.6 \div 0.7$ (Fig. 4b). In all cases Δ_{3D} is negative, signifying the fact that 3D effects reduce the albedo in the presence of absorption in all cases considered. They also enhance the absorption of incident radiation by a rough snow layer (as compared to a flat snow surface) due to more effective trapping of incident light by the surface roughness elements.

Results presented in Fig. 5 show how strongly do the 3D effects depend on the sastrugi field geometrical structure, characterized by the aspect ratio γ . The presented calculations were performed for the moderate densities $SF=0.5$; therefore, the obtained $|\Delta_{3D}|$ values can be viewed as a crude estimate of the maximum deviations when other parameters are kept fixed.

In the visible spectral region ($\omega_0=0.9999$), appearance of sastrugi leads to decrease of the snow surface albedo which, even at $\gamma=1$ (atypical for South Pole), does not exceed 10–15%, depending on sastrugi orientation relative to Sun. These results agree with the calculations of O’Rawe, performed for $\zeta_{Sun}=60^\circ$ and presented in [16]. When the snow absorptance grows, the difference between A_{3D} and A_{flat} substantially increases: e.g., at $\omega_0=0.98$, even for small surface roughness elements ($\gamma=0.01$), the albedo decrease is $\sim 15\%$; while at $\gamma=1$, the deviation $|\Delta_{3D}|$ increases to ~ 35 – 45% , depending on φ_{Sun} (Fig. 5b).

Change in the azimuth angle between the sastrugi elongation direction and incidence direction of direct solar rays from $\varphi_{Sun-sas}=0$ to $\varphi_{Sun-sas}=90^\circ$ leads to decrease of A_{3D} : for the parameters indicated in the caption of Fig. 3, it is ~ 0.03 (predominately, due to reduction of the fraction of radiation reflected from $z=0$, $A_{3D}^{(sur)}$).

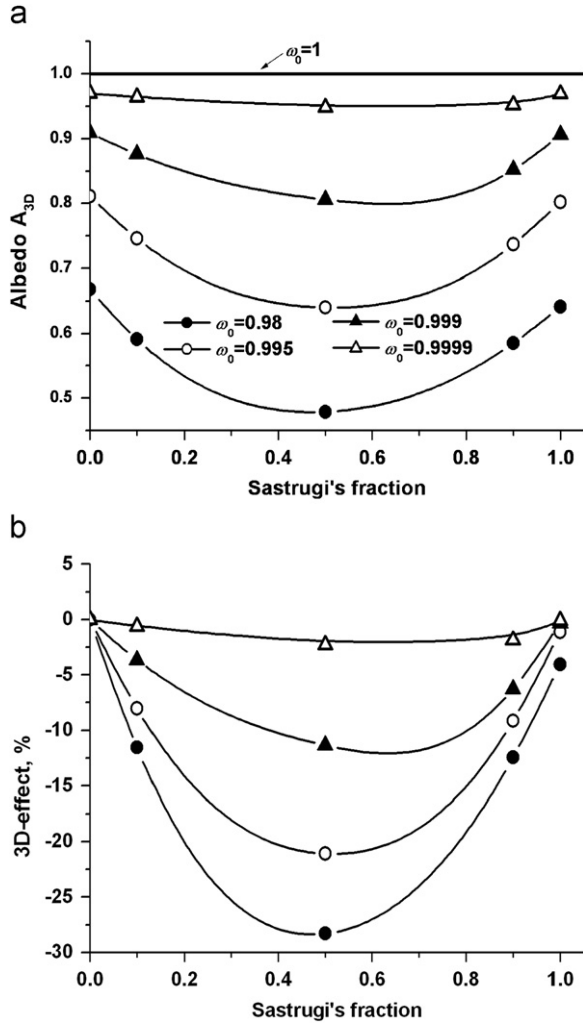


Fig. 4. The dependence of A_{3D} and A_{3D} on the sastrugi density SF for different single scattering albedos of snow; $\xi_{Sun} = 75^\circ$, and $\phi_{Sun-sas} = 90^\circ$.

6. Results of numerical simulation of the directional reflectance from a rough snow surface

6.1. Snow reflection function and anisotropic reflectance factor

The angular structure of reflected radiation will be analyzed using the snow reflection function R (3.15), as well as the anisotropic reflectance factor (ARF) ρ , defined by the formula

$$\rho(\vec{\omega}_{Sun}, \vec{\omega}_v) = R(\vec{\omega}_{Sun}, \vec{\omega}_v) / A(\vec{\omega}_{Sun}). \quad (6.1)$$

The 3D effects on SRF are studied because SRF data are employed in the algorithms of retrieval of snow grain sizes [9,59–63]. The analysis of the anisotropic reflectance factor is motivated by the fact that most works treat the angular distributions of the snow reflectance using precisely this characteristic (see, e.g., [3,16,43]). This facilitates comparison of our results against data obtained in

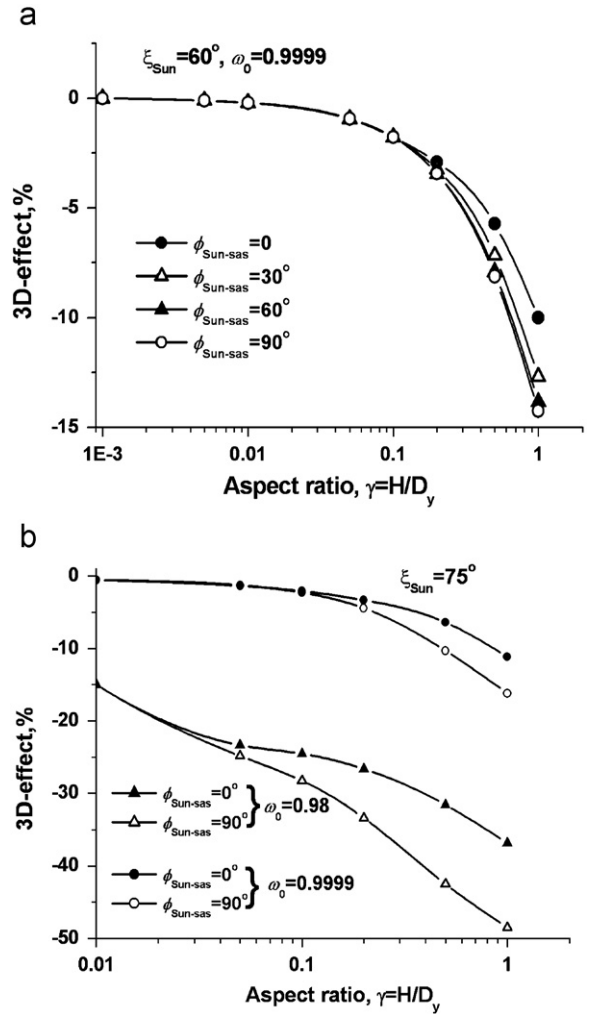


Fig. 5. The 3D effect (A_{3D}) on the snow albedo as a function of the aspect ratio $\gamma = H/D_y$ under different conditions of illumination and single scattering albedo ω_0 .

other models and experiments. Obviously, in the conservative scattering case, $\rho(\vec{\omega}_{Sun}, \vec{\omega}_v) = R(\vec{\omega}_{Sun}, \vec{\omega}_v)$.

To estimate the anisotropy, we will use henceforth ARF in the forward direction (outside of the Sun) $\rho^f = \rho(\xi_{Sun}, \xi_v, \phi_v = \phi_{Sun})$ and on antisolar side $\rho^{back} = \rho(\xi_{Sun}, \xi_v, \phi_v = \phi_{Sun} + 180^\circ)$. Analogous definitions (R^f and R^{back}) will be used to describe the SRF elongation degree.

Consider a smooth snow surface. In the solar principal plane, in the forward scattering directions, R_{flat}^f , like ρ_{flat}^f , increases as the viewing zenith angle ξ_v grows, which corresponds to decrease of the scattering angle (Figs. 6a,7a,8,9a); and in the perpendicular plane, R_{flat} and ρ_{flat} are symmetrical as functions of ξ_v (Fig. 6b). The anisotropy of the reflected radiation depends on the snow single scattering albedo: the “forward”-scattering peak ρ_{flat}^f grows as ω_0 decreases (Figs. 6a, 7b). This is because, in the visible spectral range, where the absorption by the snow grains is weak, the reflected radiation is dominated by photons experiencing more scattering events and, as such, is less anisotropic than its near-IR counterpart [64].

In the near-IR spectral channels, where absorption takes place, the photons leaving the surface of the snow cover are those which experienced, on the average, relatively small number of collisions and, hence, the scattering phase function has more significant effect on the angular structure of the reflected radiation (see also [16,26,43]).

The appearance of sastrugi leaves the *qualitative* features of the angular structure of the reflected radiation practically unchanged from the flat snow: e.g., the snow is brightest when viewed near the horizon, in the direction of the solar azimuth, and it is darkest when viewed near nadir, in the opposite direction of the solar azimuth; the ARF value grows with increase of ξ_{Sun} and decrease of ω_0 (Figs. 6–10).

The 3D effects are a reason for substantial *quantitative* differences of R_{3D} from R_{flat} . This is because the radiation, reflected by inter-sastrugi smooth surface at near-nadir viewing angles, may leave the layer A without interacting with protrusions; whereas for large ξ_v , the photons may be intercepted by sastrugi. Reflection from the flat snow is due to both direct radiation, determined by the area of the smooth surface $z=0$ not shadowed by sastrugi, and to diffuse radiation, which is reflected by inter-sastrugi sections and, in particular, by shadowed ones. Non-shadowed area is proportional to $(1-SF)$ and depends on the illumination conditions and aspect ratio γ (Appendix B). Still another factor which may influence R_{3D} and ρ_{3D} is the illumination of lateral sastrugi faces by direct solar rays and the possibility of an additional reflection of radiation by non-horizontal surfaces. As in the case of reflection from inter-sastrugi smooth surface, growth of ξ_v reduces the probability of a photon to leave a rough layer without being intercepted by other sastrugi.

We will discuss how strongly do the above-listed factors influence the change in the snow reflection function and anisotropic reflectance factor.

6.2. Influence of the sastrugi density

It should be expected that, in analogy with the snow albedo, differences between R_{flat} (ρ_{flat}) and R_{3D} (ρ_{3D}) will be maximum for moderate sastrugi densities, provided that all the other parameters of the problem are kept fixed. This is confirmed by results presented in Figs. 6 and 7: the 3D effects are most significant for $SF=0.5$, because for small ($SF=0.1$) and large ($SF=0.9$) values of SF the angular structure of the reflected radiation, like the albedo of the “flat surface–sastrugi” system, is determined by reflection from smooth surface or is formed within the layer A without interacting with smooth surface.

Under the conditions of the *conservative* scattering, the appearance of sastrugi leads to decrease of the “forward”-scattering peak R_{3D}^f in comparison with R_{flat}^f . For instance, at $SF=0.5$ and $\gamma=0.1$, the value of $R_{3D}^f(\xi_v=75^\circ) = \rho_{3D}^f(\xi_v=75^\circ)$ decreases by a factor of ~ 1.15 (~ 1.35) for $\xi_{\text{Sun}}=60^\circ$ ($\xi_{\text{Sun}}=75^\circ$) in comparison with smooth surface (Figs. 6a, 8). At the same time, in directions close to nadir and in the opposite direction of the solar azimuth for $\xi_v \leq 40^\circ$, the 3D effects lead to increase of SRF over that of smooth surface.

In the case of *moderate absorption* by snow grains ($\omega_0=0.98$), the inequality $R_{3D} < R_{\text{flat}}$ is fulfilled in the entire range of the viewing angles. At $SF=0.5$ and $\xi_v \leq 75^\circ$ with increase of the solar zenith angle from 60° to 75° , the ratio $R_{\text{flat}}^f/R_{3D}^f$ increases from ~ 1.35 to ~ 1.6 (Figs. 7a and 9a), while ARF changes to a smaller degree: at $\xi_{\text{Sun}}=60^\circ$, when $\rho_{\text{flat}}^f=2.0$ and $\rho_{3D}^f=1.88$, we have $\rho_{\text{flat}}^f/\rho_{3D}^f \approx 1.07$ (Fig. 9b); and at $\xi_{\text{Sun}}=75^\circ$, when $\rho_{\text{flat}}^f=4.35$ and $\rho_{3D}^f=3.72$, we have $\rho_{\text{flat}}^f/\rho_{3D}^f \approx 1.17$ (Fig. 7b). We note that in the case of strong absorption by snow grains, changes in the sastrugi density affect ARF much less than SRF (Figs. 6a, 7).

The results concerning the estimates of ARF in the “forward” direction are in a good agreement with data of

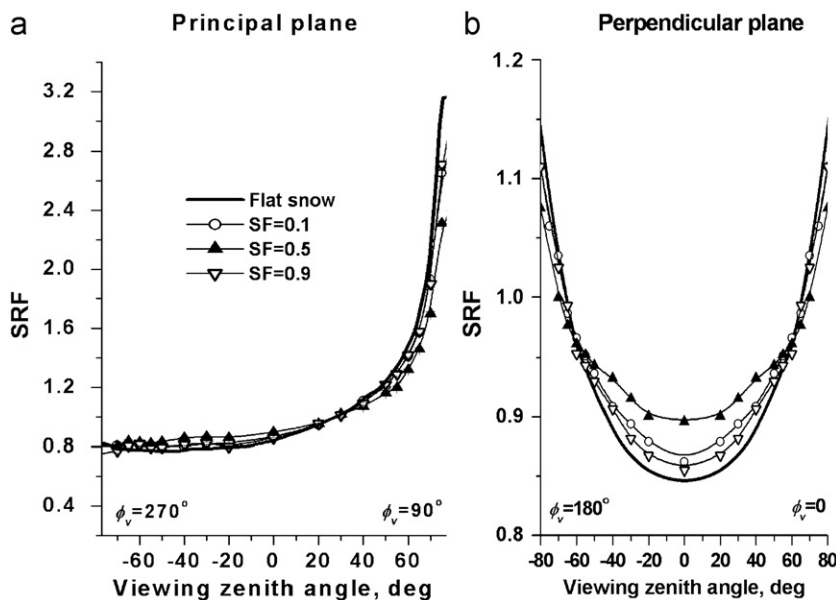


Fig. 6. Snow reflection function for SISL and rough surface as functions of the sastrugi density SF for $\xi_{\text{Sun}}=75^\circ$, $\varphi_{\text{Sun}}=90^\circ$ and $\omega_0=1$.

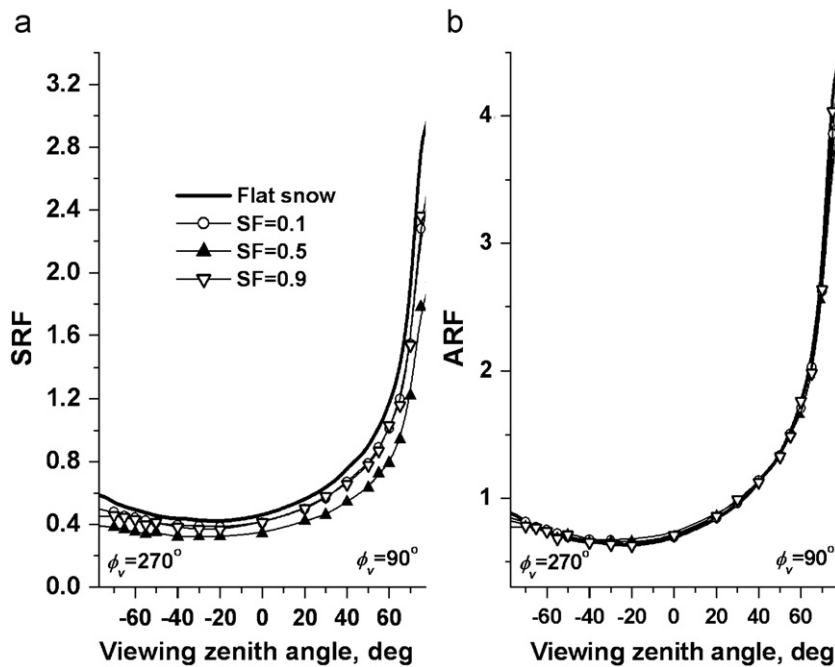


Fig. 7. Snow reflection function SRF and anisotropic reflectance factor ARF for SISL and rough surface as functions of the sastrugi density SF in the principal plane for $\xi_{\text{Sun}} = 75^\circ$, $\varphi_{\text{Sun}} = 90^\circ$ and $\omega_0 = 0.98$.

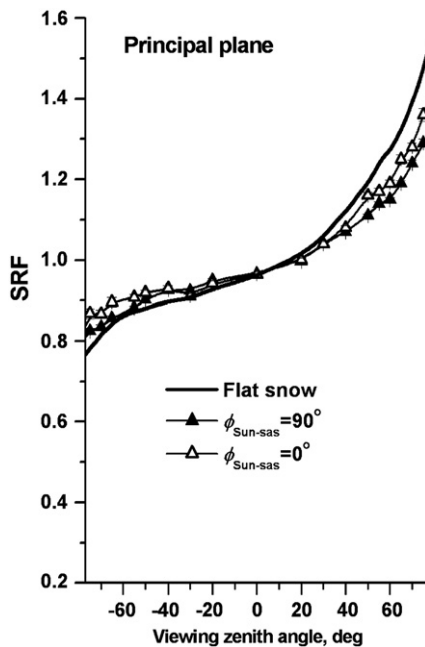


Fig. 8. Effect of sastrugi orientation on SRF for $SF=0.5$, $\xi_{\text{Sun}} = 60^\circ$ and $\omega_0 = 1$. Error bars in Figs. 8 and 9 indicate the calculation error.

simulating the reflectance from a snow surface with highly idealized sastrugi [15,16,18] and with experiments [15,16,63]. At the same time, the differences between $\rho_{\text{flat}}^{\text{back}}$ and ρ_{3D}^{back} , obtained in the Poisson model, are less than in the model calculations [15]. The results presented in [15] were obtained for small SF (the effects of

shadowing and re-reflection between sastrugi were disregarded); however, even in this case, the peak in the opposite direction of the solar azimuth substantially exceeds ARF for the smooth surface and is comparable with the “forward”-scattering peak in magnitude (Fig. 10 in [15]). At the same time, the authors of [15] state that their model overpredicts the measurements of ρ_{3D}^{back} .

The Poisson model approximates the sastrugi by rectangular parallelepipeds; therefore, the bidirectional reflectance is symmetrical in the plane perpendicular to the principal plane (Fig. 6b): $R_{3D}(\varphi_{\text{Sun}}=90^\circ, \varphi_v=0^\circ) = R_{3D}(\varphi_{\text{Sun}}=90^\circ, \varphi_v=180^\circ)$.

6.3. The effect of sastrugi orientation

Let us assume that $SF=0.5$. When solar rays are incident parallel to sastrugi ($\varphi_{\text{Sun-sas}}=0^\circ$), the radiation reflected outside of the Sun and in antisolar side directions is in a considerable degree due to reflection from inter-roughness smooth surface because the reflected radiation propagates in these directions without interaction with sastrugi. Obviously, under these conditions a substantial contribution to R_{3D} (ρ_{3D}) comes from the direct radiation reflected from $z=0$. The radiation leaving through the lateral sastrugi surfaces in these directions is small because, for a given sastrugi orientation, the incident radiation is reflected by the sections with relatively small mean area $H \times D_y$ (Fig. 1) and may be intercepted by other sastrugi.

Suppose that $\varphi_{\text{Sun-sas}}=90^\circ$ (solar rays are incident perpendicular to sastrugi). The contribution from flat surface to the snow reflectance in the solar principal plane decreases because of the increase of the shadowed area; the possibility that the lateral surfaces with the area

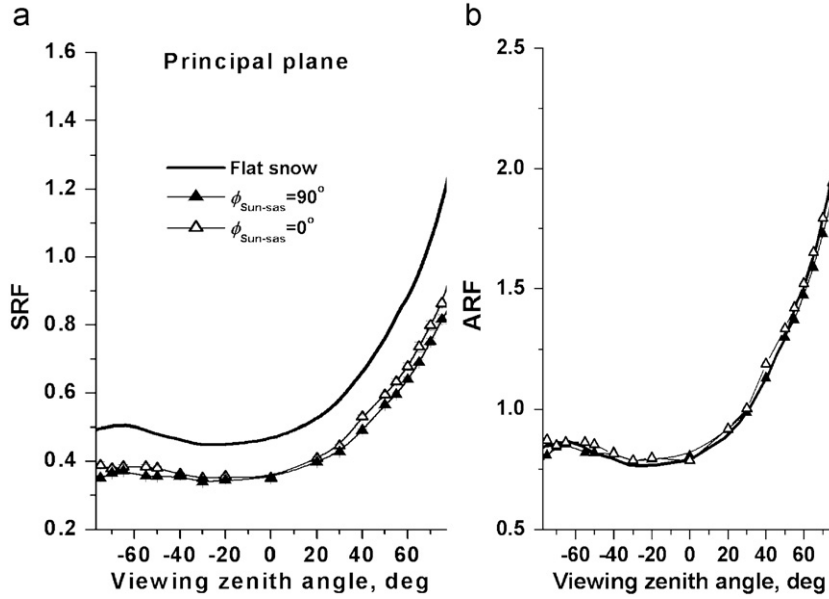


Fig. 9. Effect of sastrugi orientation on SRF and ARF for $SF=0.5$, $\xi_{\text{Sun}}=60^\circ$ and $\omega_0=0.98$.

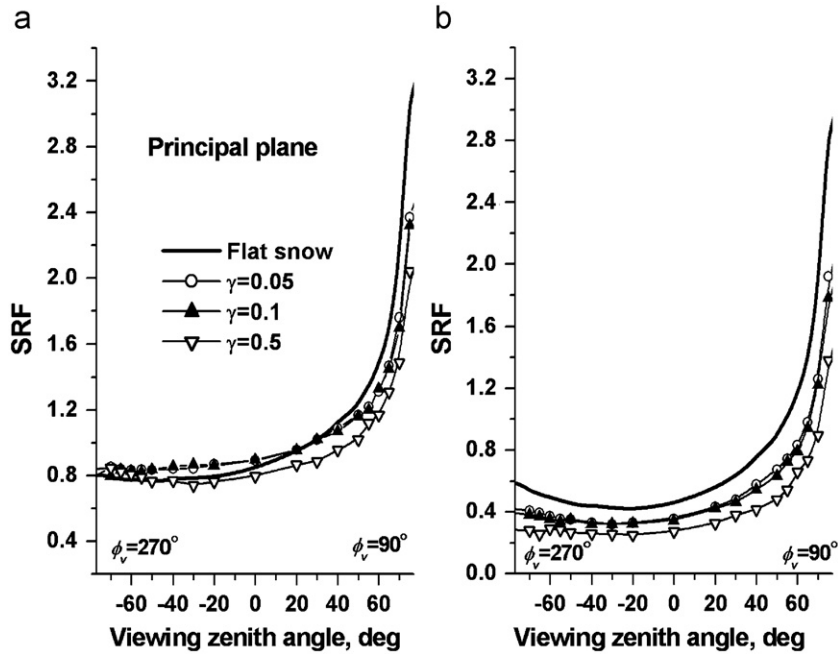


Fig. 10. Dependence of SRF on the aspect ratio γ for $SF=0.5$, $\xi_{\text{Sun}}=75^\circ$ and for (a) $\omega_0=1$ and (b) $\omega_0=0.98$.

$H \times D_x \gg H \times D_y$ are illuminated by direct solar rays depends on SF and ξ_{Sun} (Appendix B); and the probability of the radiation being intercepted by the roughnesses, as for $\phi_{\text{Sun-sas}}=0^\circ$, increases with approaching the horizon. The net result of these factors is that, in the scattering direction $\phi_v=\phi_{\text{Sun}}$ for large viewing zenith angles, the inequality $R_{3D}(\phi_{\text{Sun-sas}}=90^\circ) \leq R_{3D}(\phi_{\text{Sun-sas}}=0^\circ) \leq R_{\text{flat}}$ holds (Figs. 8, 9a).

The sastrugi orientation relative to the azimuth angle of incidence of direct solar rays affects SRF and ARF most

significantly as viewing angles approach the horizon. In the near-“nadir” direction, when the probability of a photon to leave the layer \mathcal{A} with no extra attenuation by sastrugi increases, the effect of the $\phi_{\text{Sun-sas}}$ variations on the bidirectional reflectance decreases (Figs. 8, 9).

6.4. Effect of the aspect ratio γ

To investigate the effect of the aspect ratio $\gamma=H/D_y$, we increased the geometrical height H of sastrugi

while keeping their mean horizontal sizes unchanged. Obviously, in this case the variations of γ were accompanied by increase of the optical depth ($\tau = \sigma H$), because the snow extinction coefficient remained constant. The numerical simulation was performed both for characteristic sastrugi sizes $H=5\text{--}10\text{ cm}$, and for less probable height $H=50\text{ cm}$. (We used this latter value in order to evaluate the maximum possible deviations, caused by increase of the geometrical thickness and optical depth.)

With increase of sastrugi height, the probability that line of sight along slant paths is screened by sastrugi increases, and the contribution to R_{3D} due to reflection from the underlying flat snow surface and lateral sides decreases. A consequence of this is that $R_{3D}(H=50\text{ cm})$ is less than $R_{3D}(H=5\text{--}10\text{ cm})$ practically in all range of angles in the solar principal plane (Fig. 10). We note that, at $\omega_0=1$, the reflection at “nadir” in the presence of high sastrugi $H=50\text{ cm}$ may be smaller than for the flat surface, in contrast to the typical values $H=5\text{--}10\text{ cm}$, when $R_{3D}(\xi_v=0) \geq R_{\text{flat}}(\xi_v=0)$ (Figs. 10a and 10b). Change of the aspect ratio within its typical variability range influences ARF much weaker than SRF.

7. Conclusions and outlook

In this work, we suggested a statistical approach to describe the sastrugi effects on snow-reflected solar radiation. The albedo and angular radiative characteristics, averaged over the ensemble of realizations of surface inhomogeneities, are numerically simulated in the framework of the model on the basis of Poisson point fluxes on the straight lines. The statistical homogeneity (a constant geometrical sastrugi height H) and constant optical characteristics of snow (extinction coefficient, albedo, and single-scattering phase function) were assumed, which allowed us to use the method of closed equations [20,21] to calculate the fields of the brightness and albedo of the snow cover. The smooth snow surface, on which the sastrugi were located, was approximated by flat semi-infinite snow layer, whose bidirectional reflectance was simulated beforehand using the solution of the 1-D radiative transfer equation.

The 3D effects were estimated by comparing the radiative characteristics calculated in the presence of sastrugi and SISL. The effect of sastrugi on the angular characteristics of reflected radiation was analyzed employing the snow reflection function and anisotropic reflectance factor.

In the framework of the used Poisson model, we obtained the following results:

1. The 3D effects of rough snow surface affect most appreciably the albedo and angular characteristics of the brightness field of the “flat snow–sastrugi” system at moderate ($SF \sim 0.5\text{--}0.6$) sastrugi densities and under conditions when the direct solar rays are incident perpendicular to the sastrugi elongation direction ($\varphi_{\text{Sun–sas}} = 90^\circ$).
2. When $\omega_0 < 1$, the appearance of the sastrugi leads to decrease of the albedo of the snow cover: for typical geometrical sastrugi characteristics, the maximum

relative difference between A_{3D} and A_{flat} at $\xi_{\text{Sun}} = 75^\circ$ is 2–3% when $\omega_0 = 0.9999$, increasing to $\sim 30\%$ when $\omega_0 = 0.98$.

3. A consequence of the appearance of the roughnesses is the decrease of the anisotropy of the snow surface reflectance. In particular, under the conservative scattering conditions, when $SF=0.5$, $\gamma=0.1$, and $\xi_{\text{Sun}} = \xi_v = 75^\circ$, the ρ_{3D}^f values decrease by a factor of ~ 1.35 in comparison with ρ_{flat}^f ; and near nadir and in the backscattering direction up to the viewing angles $\xi_v \leq 40^\circ$, ρ_{3D}^f exceeds ρ_{flat}^f by approximately a factor of 1.1.

The simulation results suggest that the “forward”-scattering peak in the anisotropic reflectance factor increases with growth of the solar zenith angle and snow absorptance. These results qualitatively agree with data of measurements (see, e.g., [8]). At the same time, in the Poisson model of sastrugi the peak in the “back”-scattering direction ρ_{3D}^{back} is much weaker than in ρ_{3D}^f and it is in a better agreement with experimental data, unlike model-based results [15].

4. The 3D effects have a stronger influence on SRF than on ARF. As the snow absorptance increases, the snow reflection function decreases, and at $\omega_0 = 0.98$ the inequality $R_{3D} \leq R_{\text{flat}}$ holds (in the angular interval $60^\circ \leq \xi_{\text{Sun}} \leq 75^\circ$ and at $SF=0.5$, $\gamma=0.1$ in “nadir” views, R_{flat} exceeds R_{3D} by approximately a factor of 1.3).

For large viewing zenith angles, changes of the Sun orientation relative to the sastrugi direction lead to increase of the differences in SRF between rough surface and SISL in the directions of outside of the Sun and antisolar side. The difference between $R_{3D}(\varphi_{\text{Sun–sas}}=0)$ and $R_{3D}(\varphi_{\text{Sun–sas}}=90^\circ)$ in the range $\xi_{\text{det}} \leq 20^\circ$ is much less.

Change in the relationship between R_{3D} and R_{flat} may stem from the sastrugi height: e.g., in nadir view and in the absence of the absorption, the inequality $R_{3D} > R_{\text{flat}}$, which holds when $\gamma=0.05\text{--}0.1$, is reversed at $\gamma=0.5$.

The estimates presented here show that the neglect of the snow surface roughnesses in the SRF calculations may bias snow grain size retrievals. (We note that the presented estimates pertain to situations with moderate sastrugi density $SF=0.5$, when the 3D effects are most strongly manifested.)

In conclusion, we note that the roughness effects are simulated in the framework of quite simple Poisson model, which approximates the sastrugi by rectangular parallelepipeds. The approach taken by us to calculate the radiative characteristics, in contrast to the models used earlier, makes it possible to account for the main regularities in behavior of the reflected radiation (such as to account for the effect of re-reflection of radiation by the neighboring sastrugi). At the same time, the sastrugi may be inclined due to wind effect, making, say, inclined parallelepipeds more suitable for their approximation. This would change a shadow area rather significantly, along with the magnitude of 3D effects, for a large range of solar angles. Moreover, the parameters (A_x and A_y , see Appendix A) of the Poisson model, used in these calculations, correspond to the values obtained in construction of the model of broken clouds. Passage from clouds to

sastrugi may require additional studies to refine input parameters of the Poisson model. We also note that realistic sastrugi have a rounded rather than rectangular shape of protrusion.

Nevertheless, the derived results on the directional reflectance of snow can be used as a first approximation in the problems dealing with accounting for the 3D effects on the retrieval of snow grain sizes from optical measurements (e.g., from a satellite, where 3D effects can be rarely avoided).

$$h_l(\vec{x}_n) = \begin{cases} \left[\sum_{i=1}^2 D_i \exp\{-(\eta_i |z^* - z_n|)/|\mu^*|\} g(z_n, \mu_{n-1}) \right] / |\mu^*|, & (z^* - z_n)\mu^* > 0, \mu_{n-1} = (\vec{\omega}_{n-1}, \vec{\omega}^*); \\ 0, & (z^* - z_n)\mu^* < 0; \end{cases} \quad (\text{A.4})$$

Acknowledgements

The research of T. Zhuravleva has been supported by the Program of Department of Earth Sciences of Russian Academy of Sciences (through grant 11.1) and by Russian Fund for Basic Research (through grant 09-05-963). The research of A. Kokhanovsky has been supported by the ESA Snow_Radiance Project, University of Bremen, DFG TERRA Project, BMBF CLIMSLIP Project, and S-GLI Snow Project (JAXA).

Appendix A. The average intensity and its calculation

In this section, we present formulas for calculating the average intensity $\langle I(z^*, \vec{\omega}^*) \rangle$ in the direction $\vec{\omega}^* \neq \vec{\omega}_{\text{Sun}}$ and average fluxes $\langle F(z^*) \rangle$ at the level $z = z^*$ [20,32].

Values of η_i , D_i , C_i , $i = 1, 2$, determining the generalized kernel $k(\vec{x}', \vec{x})$ and the free term $\psi(\vec{x})$ in Eqs. (3.11) and (3.12), and required to specify the Markov chain, are defined by the formulas

$$\eta_{1,2} = \{(\sigma + A(\vec{\omega})) \mp \sqrt{(\sigma + A(\vec{\omega}))^2 - 4A(\vec{\omega})P\sigma}\}/2, \\ D_1 = (\eta_2 - \sigma)/(\eta_2 - \eta_1), \quad D_2 = 1 - D_1, \quad C_1 = (\eta_2 - \sigma P)/(\eta_2 - \eta_1), \\ C_2 = 1 - C_1, \quad (\text{A.1})$$

where $A(\vec{\omega}) = A_x \times |a| + A_y \times |b|$. The intensities of the Poisson flux A_x and A_y are specified using formulas, obtained earlier for the cloud fields with random geometry [21,32–34]

$$A_x = [1.65 \times (P - 0.5)^2 + 1.04]/D_x, \quad A_y = [1.65 \times (P - 0.5)^2 + 1.04]/D_y.$$

In accordance with [31], J_h is determined by the mathematical expectation of a random quantity

$$\eta = \sum_{n=0}^{N_0} Q_n h_l(\vec{x}_n), \quad (\text{A.2})$$

where N_0 is the random number of the last state in the Markov chain, with the weights given as

$$Q_0 = 1/(2\pi), \quad Q_n = \omega_0 Q_{n-1}, \quad n \geq 1. \quad (\text{A.3})$$

The Markov chain is determined by the initial $\psi(\vec{x})$ and transition $\tilde{k}(\vec{x}', \vec{x}) = k(\vec{x}', \vec{x})/\omega_0$ probability densities as given by formulas (3.12) and (3.11), respectively.

To calculate the average flux $\langle F(z^*) \rangle = \int_{2\pi} \mu \langle I(z^*, \vec{\omega}) \rangle d\vec{\omega}$, we use a weighting function in the form $h_F(\vec{x}_n)$. Forms of the functions $h_l(\vec{x}_n)$ and $h_F(\vec{x}_n)$, $\vec{x}_n = (\vec{r}_n, \vec{\omega}_{n-1})$, depend on the spatial point \vec{x}_n , at which interaction of photon with particles of the substance occurs [32–34].

If $0 < z_n < H$ (scattering occurs inside the layer 1), then it follows that

$$h_F(\vec{x}_n) = \begin{cases} \sum_{i=1}^2 D_i \exp\{-(\eta_i |z^* - z_n|)/|\mu_n|\}, & (z^* - z_n)\mu_n > 0, \\ 0, & (z^* - z_n)\mu_n < 0; \end{cases} \quad (\text{A.5})$$

The reflectance of the underlying surface ($z_n = 0$) is described using the reflection coefficient $\rho_{\text{surf}}(\vec{\omega}_{\text{inc}}, \vec{\omega}_{\text{refl}})$. The directions of incidence $\vec{\omega}_{\text{inc}}$ and reflection $\vec{\omega}_{\text{refl}}$ are characterized by the cosines of zenith angles and by the azimuth angles:

$$\rho_{\text{surf}}(\vec{\omega}_{\text{inc}}, \vec{\omega}_{\text{refl}}) = \rho_{\text{surf}}(\mu_{\text{inc}}, \varphi_{\text{inc}}, \mu_{\text{refl}}, \varphi_{\text{refl}}). \quad (\text{A.6})$$

In the case of reflection of light from anisotropic surface, the estimation procedure includes the following steps:

1. Calculation of probability of reflection from the underlying surface $P_{\text{refl}}(\mu_{\text{inc}}, \varphi_{\text{inc}})$:

$$P_{\text{refl}}(\mu_{\text{inc}}, \varphi_{\text{inc}}) = \frac{1}{\pi} \int_0^{2\pi} \int_0^1 \rho_{\text{surf}}(\mu_{\text{inc}}, \varphi_{\text{inc}}, \mu_{\text{refl}}, \varphi_{\text{refl}}) \times \mu_{\text{refl}} d\mu_{\text{refl}} d\varphi_{\text{refl}}. \quad (\text{A.7})$$

This quantity will be used subsequently to calculate the probability density of scattering of a photon in the direction $\vec{\omega}_{\text{refl}}$ in the case of surface reflection (“scattering phase function in the case of surface reflection”)

$$g_{\text{surf}}(\mu_{\text{inc}}, \varphi_{\text{inc}}, \mu_{\text{refl}}, \varphi_{\text{refl}}) = \rho_{\text{surf}}(\mu_{\text{inc}}, \varphi_{\text{inc}}, \mu_{\text{refl}}, \varphi_{\text{refl}}) \times \mu_{\text{refl}} / (\pi P_{\text{refl}}(\mu_{\text{inc}}, \varphi_{\text{inc}})). \quad (\text{A.8})$$

2. Weight calculation:

$$Q_n = Q_{n-1} \times P_{\text{refl}}(\mu_{\text{inc}}, \varphi_{\text{inc}}). \quad (\text{A.9})$$

3. Calculation of the function $h_l(\vec{x}_n)$, to evaluate the contribution to sum (A.2) coming from the collision

point $(x_n, y_n, z_n = 0, \vec{\omega}^*)$ in the calculations of the average intensity

$$h_l(\vec{x}_n) = \left[\sum_{i=1}^2 D_i \exp(-\eta_i z^* / |\mu^*|) g_{\text{surf}}(\mu_{\text{inc}}, \varphi_{\text{inc}}, \mu^*, \varphi^*) \right] / \mu^*; \quad (\text{A.10})$$

4. Calculation of a new direction of photon travel, using “scattering phase function in the case of surface reflection” $g_{\text{surf}}(\mu_{\text{inc}}, \varphi_{\text{inc}}, \mu_{\text{refl}}, \varphi_{\text{refl}})$ (see (A.8)).

If the underlying surface is orthotropic ($\rho_{\text{surf}}(\vec{\omega}_{\text{inc}}, \vec{\omega}_{\text{refl}}) = A_s$, where A_s is the surface albedo), then, in accordance with (A.7) and (A.8),

$$P_{\text{refl}}(\vec{\omega}_{\text{inc}}) = A_s, \quad g_{\text{surf}}(\vec{\omega}_{\text{inc}}, \vec{\omega}_{\text{refl}}) = \mu_{\text{refl}} / \pi,$$

which coincides with the well-known formulas for simulating surface reflection according to Lambert law [31].

Appendix B. The area of the snow cover illuminated by the direct radiation in the presence of sastrugi

We will discuss how appearance of the sastrugi changes the area of the snow cover illuminated by the direct radiation. For simplicity, we will consider the case when sastrugi are infinite in the direction of the OX axis, have the same size D in the direction of the OY axis, and are at one and the same spacing Δ from one another (Fig. B1). We will assume that sastrugi-covered section in the direction of the OY axis has an extent S and $\varphi_{\text{Sun}} = 90^\circ$.

When sastrugi are spaced regularly, their number on the section with extent S at density SF is $S \times SF/D$; and the shadowing region L and the distance Δ between the

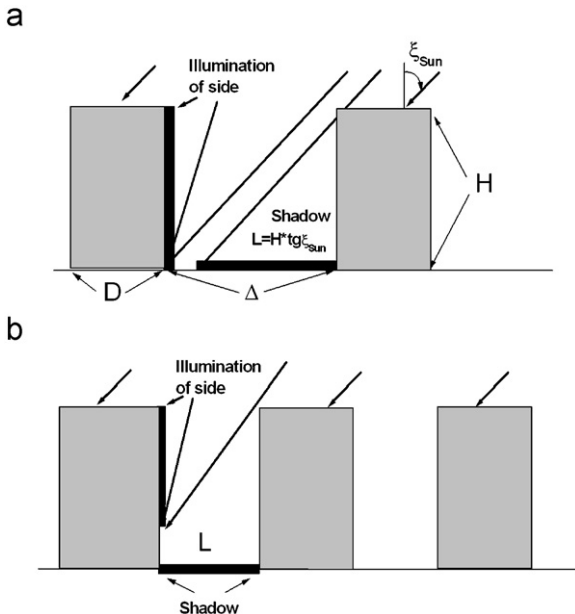


Fig. B1. Schematic illustration of solar illumination of the “underlying surface-sastrugi” system in the XOZ-plane.

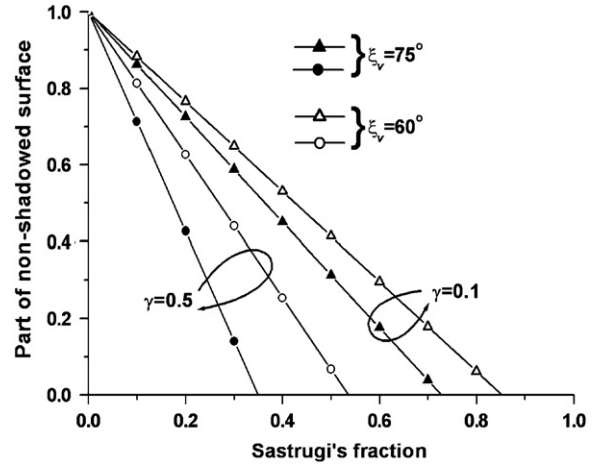


Fig. B2. Fraction of smooth surface, non-shadowed by sastrugi, as a function of sastrugi density.

sastrugi are defined by the formulas

$$L = H \times \text{tg} \xi_{\text{Sun}}, \quad \Delta = D \times (1 - SF) / SF. \quad (\text{B.1})$$

If $L \leq \Delta$ (Fig. B1a), i.e.,

$$\gamma \times SF \times \text{tg} \xi_{\text{Sun}} \leq 1 - SF, \quad \gamma = H/D, \quad (\text{B.2})$$

then a part of the smooth surface between sastrugi ($\Delta - L$) is illuminated, and side faces on the side of incidence of the solar rays are totally illuminated. Then, the illuminated area will be

$$S_{\text{sur}} = (\Delta - L) \times R \times SF/D = S \times (1 - SF - \gamma \times SF \times \text{tg} \xi_{\text{Sun}}).$$

If $L \geq \Delta$ (Fig. B2a), then sections of the underlying surface between sastrugi are completely shadowed, while the lateral faces are only partly illuminated.

As a result, the fraction of illuminated area of the smooth surface S_{sur}/S , on which sastrugi are located, will be

$$S_{\text{sur}}/S = \begin{cases} 1 - SF - \gamma \times SF \times \text{tg} \xi_{\text{Sun}}, & SF \leq SF_0 \\ 0, & SF \geq SF_0 \end{cases} \quad (\text{B.3})$$

where SF_0 is found from the condition $\Delta = L$,

$$SF_0 = 1 / (\gamma \times \text{tg} \xi_{\text{Sun}} + 1). \quad (\text{B.4})$$

Values of S_{sur}/S as functions of SF , ξ_{Sun} , and γ are presented in Fig. B2. Obviously, the fraction of non-shadowed area decreases with growth of ξ_{Sun} and with increase of the aspect ratio γ . For instance, at $\gamma = 0.1$, the smooth surface, on which sastrugi are located, is completely shadowed when $SF \approx 0.85$ at $\xi_{\text{Sun}} = 60^\circ$ and when $SF \approx 0.7$ at $\xi_{\text{Sun}} = 75^\circ$; while at $\gamma = 0.5$, complete shadowing occurs already when $SF \sim 0.35$ – 0.55 .

We note that, though obtained under assumption of a regular sastrugi spacing on the horizontal surface, the presented estimates can also be used to derive some quantitative estimates for a random roughness spacing.

References

- [1] Wiscombe WG, Warren SG. A model for the spectral albedo of snow, I. Pure snow. J Atmos Sci 1980;37:2712–33.

- [2] Painter TH, Dozier J. Measurements of the hemispherical-directional reflectance of snow at the fine spectral and angular resolution. *J Geophys Res* 2004;109:D18115.
- [3] Hudson S, Warren S. An explanation for the effect of clouds over snow on the top-of-atmosphere bidirectional reflectance. *J Geophys Res* 2007;112:D19202.
- [4] Kokhanovsky A, Zege EP. Scattering optics of snow. *Appl Opt* 2004;43:1589–602.
- [5] Jin Z, Charlock TP, Yang P, Xie Y, Miller W. Snow optical properties for different particle shapes with application to snow grain size retrieval and MODIS/CERES radiance comparison over Antarctica. *Remote Sensing Environ* 2008;112:3563–81.
- [6] Warren SG, Brandt RE, Hinton PO. 'R.: Effect of surface roughness on bidirectional reflectance of Antarctic snow. *J Geophys Res* 1998;103:25789–807.
- [7] Painter TH, Dozier J. Measurements of the hemispherical-directional reflectance of snow at fine spectral and angular resolution. *J Geophys Res* 2004;109:D18115, doi:10.1029/2003JD004458.
- [8] Hudson SR, Warren SG, Brandt RE, Grenfell TC, Six D. Spectral bidirectional reflectance of Antarctic snow: measurements and parameterization. *J Geophys Res* 2006;111:D18106, doi:10.1029/2006JD007290.
- [9] Lyapustin A, Tedesco M, Wang Y, Aoki T, Hori M, Kokhanovsky A. Retrieval of snow grain size over Greenland from MODIS. *Remote Sensing Environ* 2009;113:1976–87.
- [10] Lyapustin A, Gatebe CK, Kahn R, Brandt R, Redemann J, Russell P, et al. Analysis of snow bidirectional reflectance from ARCTAS spring-2008 campaign. *Atmos Chem Phys* 2010;10:4359–75.
- [11] Kuhn M. Anisotropic reflection from sastrugi fields. *Antarc J US* 1974;9:123–5.
- [12] Kuhn M. Bidirectional reflectance of polar and alpine snow surface. *Ann Glaciol* 1985;6:164–7.
- [13] Kuhn M, Siogas L. Spectroscopic studies at McMurdo, South Pole and Siple stations during the austral summer 1977–1978. *Antarc J US* 1978;13:178–9.
- [14] Grenfell TC, Warren SG, Mullen PC. Reflection of solar radiation by the Antarctic snow surface at ultraviolet, visible and near-infrared wavelengths. *J Geophys Res* 1994;99(D9):18669–84.
- [15] Leroux C, Fily M. Modelling the effect of sastrugi on snow reflectance. *J Geophys Res* 1998;103(E11):25779–88.
- [16] Warren SG, Brandt RE, O'Rawe P. Effect of surface roughness on bidirectional reflectance of Antarctic snow. *J Geophys Res* 1998;103(E11):25789–807.
- [17] Roujean JL, Leroy M, Deschamps PY. A bidirectional reflectance model of Earth's surface for correction of remote sensing data. *J Geophys Res* 1992;97(B18):20455–68.
- [18] O'Rawe P. Monte Carlo models for the reflection of sunlight from rough snow surfaces: Suncups and sastrugi. Master's thesis. Seattle: University of Wash; 1991.
- [19] Avaste O, Vainikko G. Calculation of the mean values of the intensities and fluxes in broken clouds. IAMAP/IAGA International Union of Geodesy and Geophysics, XV General Assembly. M; 1971.
- [20] Titov G. Statistical description of radiation transfer in clouds. *J Atmos Sci* 1990;47:24–37.
- [21] Zuev VE, Titov GA. Atmospheric optics and climate. Tomsk: Spectr; 1996 [in Russian].
- [22] Mishchenko MI. Multiple scattering, radiative transfer, and weak localization in discrete random media: Unified microphysical approach. *Rev Geophys* 2008;46:RG2003, doi:10.1029/2007RG000230.
- [23] Tishkovets VP, Jockers K. Multiple scattering of light by densely packed random media of spherical particles: dense media vector radiative transfer equation. *J Quant Spectrosc Radiat Transfer* 2006;101:54–72.
- [24] Mishchenko MI, Tishkovets VP, Travis LD, Cairns B, Dlugach JM, Liu L, et al. Electromagnetic scattering by a morphologically complex object: fundamental concepts and common misconceptions. *J Quant Spectrosc Radiat Transfer* 2010; doi:10.1016/j.jqsrt.2010.03.016.
- [25] Leroux C, Lenoble J, Brogniez G, Hovenier JW, de Haan JF. A model for the bidirectional polarized reflectance of snow. *J Quant Spectrosc Radiat Transfer* 1999;61:273–85.
- [26] Mishchenko MI, Dlugach JM, Yanovskiy EG, Zakharova NT. Bidirectional reflectance of flat, optically thick particulate layers: an efficient radiative transfer solution and applications to snow and soil surfaces. *J Quant Spectrosc Radiat Transfer* 1999;63:409–32.
- [27] Kokhanovsky AA. Light scattering media optics: problems and solutions. Chichester, U. K: Praxis; 2004.
- [28] Tanikawa T, Aoki T, Hori M, Hachikubo A, Abe O, Aniya M. Monte Carlo simulations of spectral albedo for artificial snowpacks composed of spherical and nonspherical particles. *Appl Opt* 2006;45:5310–9.
- [29] Marshak A, Davis AB. 3D radiative transfer in cloudy atmospheres. Berlin Heidelberg: Springer-Verlag; 2005.
- [30] Mikhailov GA. Optimization of weighting Monte Carlo methods. Moscow: Nauka; 1987.
- [31] Marchuk GI, Mikhailov G, Nazaraliev M, Darbinjan R, Kargin B, Elepov B. The Monte Carlo methods in atmospheric optics. New York: Springer-Verlag; 1980.
- [32] Titov GA, Zhuravleva TB, Zuev VE. Mean radiation fluxes in the near-IR spectral range: Algorithms for calculation. *J Geophys Res* 1997;102(D2):1819–32.
- [33] Zhuravleva TB. Statistical simulation of propagation of solar radiation: Determinate atmosphere and stochastic clouds. Doctoral Dissertation, 2008. Tomsk: Institute of Atmospheric Optics SB RAS, Russia [in Russian].
- [34] Zhuravleva TB. Simulation of solar radiative transfer under different atmospheric conditions. Part II. Stochastic clouds. *J Atmos Ocean Opt* 2008;21:163–75.
- [35] Gay M, Fily M, Genthon C, Frezzotti M, Oerter H, Winther J-G. Snow grain-size measurements in Antarctica. *J Glaciol* 2002;48(N163):527–35.
- [36] Li S, Zhou X. Modelling and measuring the spectral bidirectional reflectance factor of snow-covered sea ice: an intercomparison study. *Hydrol Process* 2004;18:3559–81.
- [37] Domine F, Albert M, Huthwelker T, Jacobi H-W, Kokhanovsky AA, Lehning M, et al. Snow physics as relevant to snow photochemistry. *Atmos Chem Phys Discuss* 2007;7:5941–6036.
- [38] Fily M, Leroux C, Lenoble J, Sergeant C. Terrestrial snow studies from remote sensing in the solar spectrum and in the thermal infrared. *Atmosph Space Sci Lib* 1998;227:421–41.
- [39] Grenfell TC, Warren SG. Representation of nonspherical ice particle by a collection of independent spheres for scattering and absorption of radiation. *J Geophys Res* 1999;104(D24):31697–709.
- [40] Nolin AW, Dozier J. Estimating snow grain size using AVIRIS data. *Remote Sensing Environ* 1993;44:231–8.
- [41] Nolin AW, Dozier J. A hyperspectral method for remotely sensing the grain size of snow. *Remote Sensing Environ* 2000;74:207–16.
- [42] Flanner MG, Zender CS. Linking snowpack microphysics and albedo evolution. *J Geophys Res* 2006;111:D12208.
- [43] Leroux C, Deuze JL, Goloub P, Segent C, Fily M. Ground measurements of polarized bidirectional reflectance of snow in the near-infrared spectral domain: comparison with model results. *J Geophys Res* 1998;103:19721–31.
- [44] Stroeve JC, Nolin AW. New methods to infer snow albedo from MISR instrument with applications to the Greenland ice sheet. *IEEE Trans Geosci Remote Sensing* 2002;40:1616–25.
- [45] Xie Y, Yang P, Gao B-C, Kattawar GW, Mishchenko MI. Effect of ice crystal shape and effective size on snow bidirectional reflectance. *J Quant Spectrosc Radiat Transfer* 2006;100:457–69.
- [46] Yang P, Liou KN. A geometric-optics/integral-equation method for light scattering by nonspherical ice crystals. *Appl Opt* 1996;35:6568–84.
- [47] Macke A, Francis PN, McFarquhar GM, Kinne S. The role of ice particle shapes and size distributions in the single scattering properties of cirrus clouds. *J Atmos Sci* 1998;55:2874–83.
- [48] Massom RA, Eicken H, Haas C, Jeffries MO, Drinkwater MR, Sturm M, et al. Snow on Antarctic sea ice. *Rev Geophys* 2001;39(3):413–45.
- [49] Munneke KP, Reijmer CH, van den Broeke MR, König-Langlo G, Stammes P, Knap WH. Analysis of clear-sky Antarctic snow albedo using observations and radiative transfer modeling. *J Geophys Res* 2008;113:D17118.
- [50] Macke A, Mueller J, Raschke E. Single scattering properties of atmospheric ice crystals. *J Atmos Sci* 1996;53:2813–25.
- [51] Sturm M, Morris K, Massom R. The winter snow cover of the West Antarctic pack ice: its spatial and temporal variability. Antarctic sea ice: physical processes, interactions and variability. *Antarct Res Ser* 1998;74:19–40.
- [52] Welch RM, Wielicki BA. Reflected fluxes for broken clouds over a Lambertian surface. *J Atmos Sci* 1989;46(10):1384–95.
- [53] Lane D, Goris E, Somerville R. Radiative transfer through broken clouds: observations and model validation. *J Climate* 2002;15(20):2921–33.
- [54] Nikolaeva OV, Bass LP, Germogenova TA, Kokhanovsky AA, Kuznetsov VS, Mayer B. The influence of neighboring clouds on the clear sky reflectance studied with the 3-D transport code RADUGA. *J Quant Spectrosc Radiat Transfer* 2005;94:405–24.

- [55] Kokhanovsky AA, Mayer B, Rozanov VV, Wapler K, Burrows JP, Schumann U. The influence of broken cloudiness on cloud top height retrievals using nadir observations of backscattered solar radiation in the oxygen A-band. *J Quant Spectrosc Radiat Transfer* 2007;103:460–77.
- [56] Zhuravleva TB, Marshak AL. On the Validation of the Poisson Model of Broken Clouds. *Izv AN. Atmos and Ocean Phys* 2005;41:713–25.
- [57] Cahalan R, Oreopoulos L, Marshak A, Evans KF, Davis A, Pincus R, et al. The International Intercomparison of 3D Radiation Codes (I3RC): Bringing together the most advanced radiative transfer tools for cloudy atmospheres. *Bull Am Meteorol Soc* 2005;86:1275–93.
- [58] Loeb NG, Várnai T, Winker DM. Influence of subpixel-scale cloud-top structure on reflectances from overcast stratiform cloud layer. *J Atmos Sci* 1998;55(18):2960–73.
- [59] Polonsky IN, Zege EP, Kokhanovsky AA, Katsev IL, Prikhach AS. The retrieval of the effective radius of snow grains and control of snow pollution with GLI data. *Geoscience and Remote Sensing Symposium, IGARSS '99 Proceedings, IEEE 1999 International*, 2, 28 June–2 July 1999, vol. 2, p. 1071–3. doi:10.1109/IGARSS.1999.774536.
- [60] Painter TH, Dozier J, Roberts DA, Davis RE, Greene RO. Retrieval of subpixel snow-covered area and grain size from imaging spectrometer data. *Remote Sensing Environ* 2003;85:64–77.
- [61] Tedesco M, Kokhanovsky A. The semi-analytical snow retrieval algorithm and its application to MODIS data. *Remote Sensing Environ* 2007;110:317–31.
- [62] Stamnes K, Li W, Eide H, Aoki T, Hori M, Stordvold R. ADEOS-II/GLI snow/ice products—Part I: scientific basis. *Remote Sensing Environ* 2007;111:258–73.
- [63] Zege EP, Katsev IL, Malinka A, Prikhach AS, Polonsky IN. New algorithm to retrieve the effective snow grain size and pollution amount from satellite data. *Annals of Glaciology* 2008;49:139–44.
- [64] Kokhanovsky AA, Aoki T, Hachikubo A, Hori M, Zege EP. Reflective properties of natural snow: approximate asymptotic theory versus in situ measurements. *IEEE Trans Geosci Remote Sensing* 2005;43:1529–35.